RSC Advances

PAPER

View Article Online
View Journal | View Issue

Cite this: *RSC Adv.*, 2022, **12**, 15526

Correlating the effect of preparation methods on the structural and magnetic properties, and reducibility of $CuFe_2O_4$ catalysts

Rattabal Khunphonoi,[a] Pongtanawat Khemthong, *[bcd] Chuleeporn Luadthong,[b] Sanchai Kuboon, [b] Chanapa Kongmark, [e] Nawin Viriya-empikul,[f] Pinit Kidkhunthod,[cg] Supree Pinitsoontorn [h] and Kajornsak Faungnawakij *[b]

$CuFe_2O_4$ spinel oxide has attracted research interest because of its versatile practical applications, especially for catalysis. In this study, nanometre-sized $CuFe_2O_4$ particles were prepared by three different methods, including nanospace confinement in SBA-15, hard template removal, and sol–gel combustion. The relationship between structure, size, magnetic behaviour, and reducibility of the catalysts was further investigated by various advanced techniques. Samples prepared by impregnation and hard template removal show high surface area and small crystallite size with superparamagnetic behaviour. In contrast, the sol–gel sample exhibits ferromagnetic properties with a large crystallite size and low surface area. Although all samples present a tetragonal crystal structure, the distributions of Fe and Cu cations in tetrahedral and octahedral sites in the spinel structure are different. The reducibility results demonstrate that the supported $CuFe_2O_4$/SBA-15 shows the lowest reduction profile. These results could suggest that the synthesis method strongly affects the crystal properties and cation distribution in the spinel structure, microstructure, surface area and reducibility, which are among the most relevant physicochemical properties for the catalytic activity.

Received 16th March 2022
Accepted 15th May 2022

DOI: 10.1039/d2ra01708c

rsc.li/rsc-advances

1. Introduction

Copper spinel oxides have long attracted attention of researchers because their structural property is suitable for use as precursors or model catalysts.[1–4] The structure of copper spinel provided excellent performance in the degradation of oxy-hydrocarbons at relatively lower temperatures of 200–350 °C, compared to other types of Cu-based catalysts.[2,5] A series of Cu-spinel species of $CuMn_2O_4$,[6] ZrO_2–$CuZn(Al_2O_3)$,[7] and $CuFe_2O_4$–SiO_2 catalysts[1] have been investigated lately. Among them, $CuFe_2O_4$ is considered to be a promising catalyst for methanol steam reforming because of the abundance of Cu and Fe in nature[8] and its active ability for hydrogen production. However, the $CuFe_2O_4$ spinel catalysts typically possessed low surface area and their copper particles became sintered after high temperature calcination, resulting in insufficient active sites. It is well known that the activity of $CuFe_2O_4$ spinel is greatly dependent on Cu particle size and its dispersion. Well dispersed Cu particles with a slow rate of sintering can promote high hydrogen production yield.

We recently examined $CuFe_2O_4$ catalysts prepared by a urea–nitrate combustion method for dimethyl ether steam reforming and found that these catalysts were highly active in spite of their low surface area.[2,9] Nevertheless, the $CuFe_2O_4$ spinel in the form of nanopores and nanoparticles should be developed to provide a new structure with higher surface area, leading to better catalytic performance. A common method to meet this requirement is impregnating mesoporous silica powders with the desired salt precursors. A hard template for crystal growth of porous metal spinel oxide is also one of many interesting techniques for preparing high surface area materials, especially mesoporous metal oxides.[10] Both methods have been used as a powerful strategy for producing crystalline nanoporous materials having a vast potential for applications in the

[a]*Department of Environmental Engineering, Khon Kaen University, Khon Kaen 40002, Thailand*

[b]*National Nanotechnology Center (NANOTEC), National Science and Technology Development Agency (NSTDA), Pathumthani 12120, Thailand. E-mail: pongtanawat@nanotec.or.th; kajornsak@nanotec.or.th*

[c]*Reaserch Network NANOTEC-SUT on Advanced Nanomaterials and Characterization, Suranaree University of Technology, 111 University Avenue, Muang, Nakhon Ratchasima 30000, Thailand*

[d]*Center of Excellence in Environmental Catalysis and Adsorption, Thammasat University, Pathum Thani, 12120, Thailand*

[e]*Specialized Center of Rubber and Polymer Materials in Agriculture and Industry, Department of Materials Science, Faculty of Science, Kasetsart University, Bangkok, Thailand*

[f]*Joint Graduate School of Energy and Environment, King Mongkut's University of Technology Thonburi, Bangkok, Thailand*

[g]*Synchrotron Light Research Institute (Public Organization), 111 University Avenue, Muang, Nakhon Ratchasima 30000, Thailand*

[h]*Integrated Nanotechnology Research Center, Department of Physics, Faculty of Science, Khon Kaen University, Khon Kaen 40002, Thailand*

catalysis.[11–13] Some advanced techniques as a block copolymer templates have been demonstrated for controlling the size, morphology, and shape of nanoparticles.[14–16] To the best of our knowledge, however, there are a few studies reporting on the relationship between structure, magnetic behaviour, and reduction behaviour of $CuFe_2O_4$ spinel prepared with different methods. Thus, in this research, the relationships of those behaviours have been examined. We have expected that this investigation could provide an information for preparing a suitable catalyst, regarding to a significant role of preparation methods on structural behaviour and catalytic performance of $CuFe_2O_4$ catalysts.

2. Experimental

2.1 Catalyst preparation

2.1.1 Impregnation and template removal method. Mesoporous SBA-15 silica template was synthesized according to method described in ref. 17. Short descriptions of method were briefly discussed as follows; 4 g of pluronic P-123 (Sigma Aldrich) was added to 130 mL of H_2O and 20 mL of 1 M hydrochloric acid (HCl, 37%). Stirred until complete dissolution. Then, approximately 9 mL of tetraethylorthosilicate (TEOS, sigma Aldrich, 98%) was added to the solution and stirred for 7.5 h at 45 °C. After that, the sample was aged at 80 °C for 15.5 h without stirring, cooled down to room temperature, filtered, washed, and calcined at 550 °C for 6 h with a heating rate of 1 °C min^{-1} in ambient atmosphere.

The $CuFe_2O_4$/SBA-15 was prepared by impregnation method using nitrate solutions of Cu and Fe with a 0.4 molar ratio.[8] Firstly, the nitrate salts were dissolved in 0.8 mL of deionized (DI) water and placed in a vacuum oven at room temperature for 1 h. The powder of mesoporous SBA-15 was slowly added to the mixed nitrates solution and stirred until the mixture became homogenized (the total weight ratio of nitrate salts and mesoporous SBA-15 was 1 : 1). Later on, the mixture was placed on hot plate at 70 °C for 1 h, ground and dried in vacuum oven overnight. After that, the red sample was calcined at 750 °C for 15 h with heating rate of 1 °C min^{-1} (the final metal loading was 27% wt. and denoted as $CuFe_2O_4$/SBA-15).

2.1.2 Hard template removal method. The mesoporous SBA-15 template of $CuFe_2O_4$/SBA-15 was eliminated by washing in 50 mL of 2 M NaOH for three times. The residue metal oxides were further centrifuged and washed with 100 mL of 95% ethanol three times. The solid metal oxide was dried at 100 °C overnight. The red-brown product was obtained, denoted as $CuFe_2O_4$_TP.

2.1.3 Sol–gel combustion method. The sol–gel combustion with a citric acid complex method was employed in this work.[5] $Cu(NO_3)_2 \cdot 2.5H_2O$ (Ajax, 98%) and $Fe(NO_3)_3 \cdot 9H_2O$ (Ajax, 98%) were dissolved in DI water and stirred continuously at 60 °C for 2 h. The mixture was added by excess amount of citric acid (Ajax, 98%) and kept stirring for 1 h. After that, the solution was heated up to 100 °C to evaporate water, then combusted at 200 °C until the reaction was completed. The combusted sample was calcined under air atmosphere at 750 °C for 15 h with a heating rate of 3 °C min^{-1}, denoted as $CuFe_2O_4$_SG.

2.2 Characterizations

The phase and crystallinity of samples were confirmed by powder X-ray diffraction (XRD; Bruker, D8 ADVANCE) with Cu K_α radiation at 40 kV and 40 mA, increment of 0.02° per second, step time of 0.5 s over the scan range of $10° < 2\theta < 80°$. The specific surface area and pore volume were determined using nitrogen adsorption–desorption isotherm technique (Bel, Belsorp-max) at 77 K. Each sample was outgassed overnight at 300 °C before measuring. The reduction profiles were carried out using temperature-programmed reduction (TPR; Quantachrome Instruments, CHEMBET-Pulsar). About 25 mg of the calcined catalyst was heated under atmosphere of 5% H_2/Ar with 10 °C min^{-1} heating rate and 30 mL min^{-1} flow rate to final temperature of 800 °C. The morphologies of the catalysts were examined with transmission electron microscopy (TEM; JEOL, JEM-2100). The samples were dispersed in methanol media and then deposited on a Cu grid. Magnetic hysteresis loops were recorded at room temperature using a vibrating sample magnetometry (VSM; LAKE SHORE VSM 7404, Lake Shore Cryotronics, Inc., USA) with a maximum magnetic field of 10 kG. The geometry, local environment, and structural properties of $CuFe_2O_4$ were solved by X-ray absorption spectroscopy (XAS) technique. Transmission XAS spectra were collected at Fe and Cu K-edges at the SUT-NANOTEC-SLRI XAS beamline (BL5.2; electron energy of 1.2 GeV; bending magnet; beam current of 80–150 mA; 1.1 to 1.7×10^{11} photon per s) of the Synchrotron Light Research Institute, Public Organization, Thailand.[18] For the acquisition of all spectra, a Ge (220) double crystal monochromator with an energy resolution ($\Delta E/E$) of 2×10^{-4} was used. Energy calibrations were carried out using Fe foil (7112 eV) and Cu foil (8979 eV). In the X-ray absorption near edge structure (XANES) region, the step size was 0.02 eV with a second integration time. The extended X-ray absorption fine structure (EXAFS) region was set to scan to the maximum of 10k. The data reduction and EXAFS curve fitting were performed using the Athena and Arthemis programs which are included in an IFEFFIT package.[19,20]

2.3 Methanol steam reforming evaluation

The catalytic activity of the prepared catalysts was demonstrated for methanol steam reforming using a tubular reactor under atmospheric pressure. A 0.2 g of each catalyst was packed in a tubular quartz cell and sandwiched with quartz wool on both sides then placed inside the furnace. Prior to the experiments, the catalyst was reduced in 10% H_2 balanced with N_2 at 350 °C with a flow rate of 40 mL min^{-1} for 3 h. After the reduction was completed, the temperature was maintained at 200 °C under N_2 flow. A mixture of methanol and steam (steam/carbon ratio = 2) was injected to a pre-heater at 150 °C to generate a gas feed stock using syringe pump with an injection rate of 100 mL min^{-1}. After that, the gas feed stock was introduced through the reactor by N_2 carrier gas with a flow rate of 100 mL min^{-1}. The reaction temperature was held in a range of 200–375 °C. The derived gaseous products in the supplied and reformed gases after experiment were collected at 3 °C using a condenser. The gas compositions were analyzed by online gas

chromatography (GC) equipped with a thermal conductivity detector (VARIAN, CP-4900). A Poraplot U column was used to separate methanol, and CO_2. A capillary molecular sieve 5 Å column was applied for H_2, O_2, N_2, CH_4, and CO separations. The catalytic activity was evaluated by the H_2 production rate.

3. Results and discussion

3.1 Characterization of $CuFe_2O_4$ catalyst

3.1.1 Formation of $CuFe_2O_4$ spinel. The XRD patterns of all samples are displayed in Fig. 1. Fig. 1(A) shows low-angle XRD patterns of the SBA-15 and $CuFe_2O_4$/SBA-15 composite. It was found that the SBA-15 exhibited typical reflection of 2θ in the region between 0.8° and 2.5° corresponding to *d*-spacing of (100), (110), (200) and (210) ascribed to the *d* values (*d* defined as a distance between the empty pore space and the wall pore) of 10.2 nm, 6.0 nm, 5.3 nm, and 4.0 nm, respectively. These reflections possessed the 2D hexagonally structural pores belonging to *P6mm* space group of an ordered mesoporous silica.[17,21] The ordered hexagonal tunnels remained after pores filling of metal precursors and further calcination under severe condition. It is noteworthy to mention that some spinel $CuFe_2O_4$ species possibly formed and grew inside the pores, leading to the reduction of SBA-15 diffraction peaks. The assumption was confirmed by the observed shrinkage of the spacing distances of (100), (110), and (200) which were equal to 9.8 nm, 5.9 nm, and 5.1 nm, respectively.

Fig. 1(B) shows wide-angle XRD spectra of calcined samples with different preparation methods. Most of the diffraction peaks corresponded to the spinel phase of $CuFe_2O_4$, manifested by the sharp characteristic reflection planes. This lattice parameter for tetragonal spinel $CuFe_2O_4$ is in good agreement with that previously reported.[22] In addition, XRD peaks of copper oxides and iron oxides were not detected in any samples. This would indicate that the synthesis methods were feasible to effectively prepare a pure $CuFe_2O_4$ phase. The catalyst prepared *via* sol–gel method showed sharp and intense reflection peaks. This was probably due to particle agglomeration during calcination. On the other hand, the XRD patterns of $CuFe_2O_4$/SBA-15 composite and $CuFe_2O_4$_TP show much broader peaks. Overlapping peaks of XRD profiles were evident and became dominant. This discernible feature indicated that small crystalline sizes without sintering of spinel oxides were formed, comparing to the sol–gel method. It should be noted that the SBA-15 has promoted and assisted the dispersion of $CuFe_2O_4$ on the surface. A closer look at these XRD peak profiles reveals a sharp 004 reflection which would suggest that the SBA-15 may favor the growth of $CuFe_2O_4$ crystal along one direction. The structure of spinel oxide ($CuFe_2O_4$_TP) was also maintained after leaching out of SBA-15. In addition, the SBA-15 did not present any diffraction patterns at high angles due to its amorphous nature of pore walls.

3.1.2 Morphology of $CuFe_2O_4$ spinel. To support our previous statements about pore filling, structure collapsing, and particle agglomeration, we have verified our inquisition by using TEM technique. Fig. 2 depicts the TEM images of SBA-15, $CuFe_2O_4$/SBA-15 and $CuFe_2O_4$ spinel synthesized with a sol–gel combustion and a template removal method. From the result, Fig. 2(A) displays a clear image of regular hexagonal pore array and empty mesopores SBA-15. The TEM image of $CuFe_2O_4$/SBA-15 (Fig. 2(B)) revealed the periodic nature of the pores, indicating that the structure of materials remained. Homogeneous dispersion of $CuFe_2O_4$ on SBA-15 was observed. The $CuFe_2O_4$ particles after leaching out the SBA-15 in NaOH solution exhibited small needle-like clusters with small particles dispersed on the surface (Fig. 2(C)). This one-dimensional growth of $CuFe_2O_4$ nanocrystals was in good agreement with the XRD results as a broad peak was observed. In contrast, the particles in the sol–gel combustion sample were sintered and fully formed a large crystalline (Fig. 2(D)). This can ascribe to the fact that the mesoporous SBA-15 would protect particle growth during the synthesis process by stabilizing and

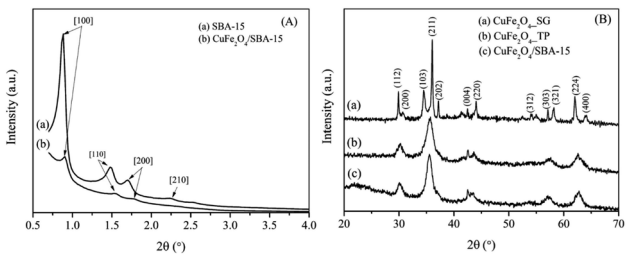

Fig. 1 (A) Low angle-XRD patterns of SBA-15 and $CuFe_2O_4$/SBA-15 composite; (B) wide angle-XRD patterns of $CuFe_2O_4$/SBA-15, $CuFe_2O_4$_TP and $CuFe_2O_4$_SG.

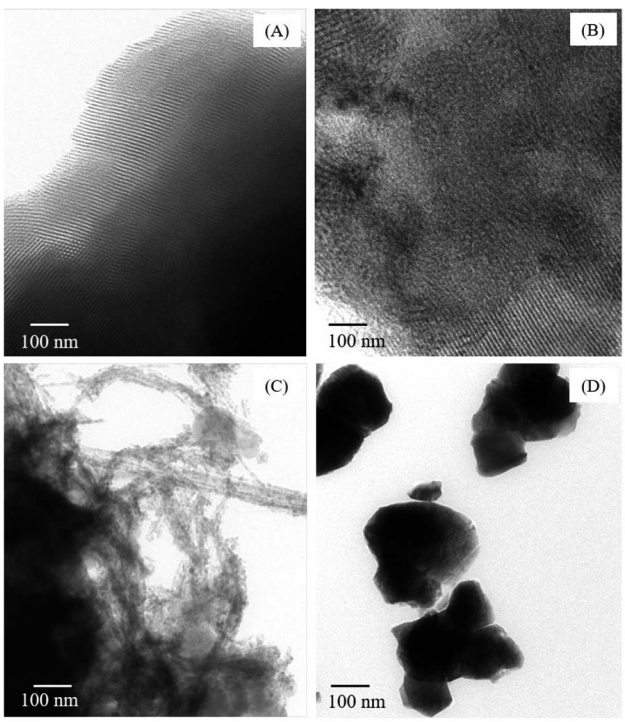

Fig. 2 TEM images of (A) SBA-15, (B) $CuFe_2O_4$/SBA-15, (C) $CuFe_2O_4$_TP and (D) $CuFe_2O_4$_SG.

prohibiting agglomeration of $CuFe_2O_4$. However, Fig. 2(B) demonstrates the incomplete pore filling of SBA-15 by $CuFe_2O_4$. This result was in good agreement with the XRD pattern where the intensity of peaks could even vanish if pores were totally filled. Thus, the bright spots represented the pores of SBA-15, which were not filled with the $CuFe_2O_4$ particles. In addition, the incomplete pore filling is due to the faster ramping rate of calcination temperature that led to building up pressure from the decomposition of precursor, hence, the capillary flow of the melting precursor salts into the mesoporous of SBA-15 silica template was restrained.[10,11]

3.1.3 BET surface area analysis of $CuFe_2O_4$ spinel. The textural properties of materials were performed using N_2-sorption isotherm and displayed in Fig. 3. The BET surface area of the synthesized catalysts is tabulated in Table 1. From the result, the N_2 sorption isotherms of $CuFe_2O_4$/SBA-15 composite displays a typical type IV adsorption according to IUPAC classification. A capillary condensation at a relative pressure of 0.5–0.9 was attributed to hysteresis loop type H1, evidently the mesoporosity of materials compared to SBA-15.[23] The $CuFe_2O_4$/SBA-15 composite possessed a lower surface area than SBA-15, which is probably due to partial filling of mesopores during the generation of spinel oxide as illustrated in the TEM images. In case of spinel oxide samples, the isotherms of $CuFe_2O_4$_TP and $CuFe_2O_4$_SG were significantly different from $CuFe_2O_4$/SBA-15 composite due to drastic reduction of the surface area. There is; however, a small hysteresis loop with isotherm being shifted to the high relative pressure for $CuFe_2O_4$_TP confirmed a mesoporous type of material. This could suggest that some parts of the space occupied by siliceous SBA-15 were removed and a broad space between needle-like spinel oxide was created, resulting in its higher surface area when compared with $CuFe_2O_4$ synthesized by sol–gel combustion.[8] It could be claimed that the template method was favourable for maintaining the nanocrystallite size with porosity even when the template was removed.

3.1.4 Magnetization of $CuFe_2O_4$ spinel. The magnetic hysteresis loops of samples with different preparation methods are also investigated to evaluate finite size effects (the high surface-to-volume ratio, different crystal structures and magnetic nanoparticles) on their catalytic activity. The surface-to-volume ratio of the nanoparticles show more significant effect on chemical reactivation rate compared to that of the corresponding bulk material.[24] Normally, the surface magnetization depends on the size of the particle contributed by the surface uncompensated spins. From Fig. 4, the result revealed that only the $CuFe_2O_4$_SG sample exhibited the magnetic hysteresis loops, while the $CuFe_2O_4$_TP and $CuFe_2O_4$/SBA-15 samples showed superparamagnetic curves at room

Table 1 BET and structural parameters obtained from EXAFS data for the three calcined $CuFe_2O_4$ catalysts[a]

Sample name	Paths	N	Occupancy (%)	R (Å)	σ^2	BET* ($m^2\ g^{-1}$)
$CuFe_2O_4$_SG	Fe–O_{1octa}	2.8	48.2	1.96	0.006	1
	Fe–Fe_{octa}	2.8		2.92	0.009	
	Fe–Cu_{octa}	2.8		3.37	0.003	
	Fe–O_{2octa}	2.8		3.38	0.009	
	Fe–O_{1tetra}	2.1	51.8	2.05	0.020	
	Fe–Fe_{tetra}	3.2		3.63	0.004	
	Fe–Cu_{tetra}	3.2		3.82	0.009	
	Fe–O_{2tetra}	6.5		3.86	0.040	
$CuFe_2O_4$_TP	Fe–O_{1octa}	3.8	63.4	1.96	0.002	30
	Fe–Fe_{octa}	3.8		2.94	0.009	
	Fe–Cu_{octa}	3.8		3.41	0.004	
	Fe–O_{2octa}	3.8		3.47	0.004	
	Fe–O_{1tetra}	1.5	36.6	1.84	0.002	
	Fe–Fe_{tetra}	2.2		3.73	0.004	
	Fe–Cu_{tetra}	2.2		3.92	0.004	
	Fe–O_{2tetra}	4.4		3.83	0.004	
$CuFe_2O_4$/SBA-15	Fe–O_{1octa}	5.1	84.3	1.96	0.014	336
	Fe–Fe_{octa}	5.1		2.98	0.001	
	Fe–Cu_{octa}	5.1		3.39	0.004	
	Fe–O_{2octa}	5.1		3.44	0.027	
	Fe–O_{1tetra}	0.6	15.7	1.96	0.001	
	Fe–Fe_{tetra}	0.9		3.64	0.002	
	Fe–Cu_{tetra}	0.9		3.52	0.011	
	Fe–O_{2tetra}	1.9		3.69	0.002	

[a] Where N = coordination number, R = distance to neighboring atom, * SBA-15 = 685 $m^2\ g^{-1}$.

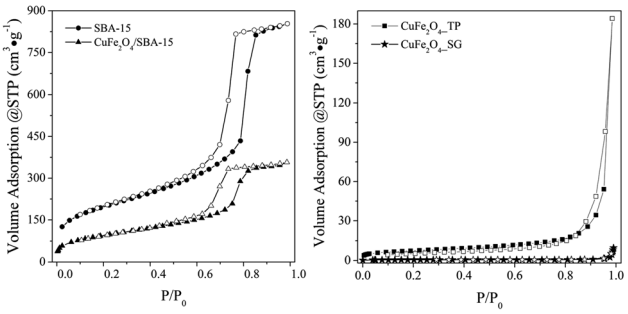

Fig. 3 N_2 adsorption–desorption isotherms of spinel and SBA-15 samples; adsorption (black) and desorption (white).

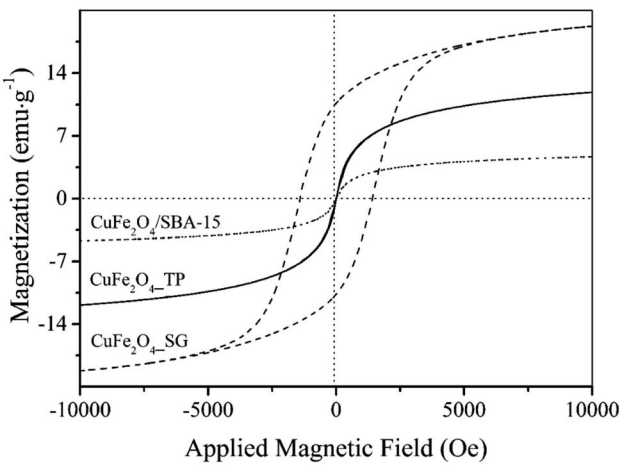

Fig. 4 Characteristic hysteresis curves of magnetization (M) *versus* applied magnetic field (H) for calcined $CuFe_2O_4$/SBA-15, $CuFe_2O_4$_TP, and $CuFe_2O_4$_SG.

temperature. This result agrees well with the results reported by Laokul *et al.*[25] and Yadav *et al.*[26] According to XRD and TEM results, the particle sizes of the $CuFe_2O_4$ species in $CuFe_2O_4$_TP and $CuFe_2O_4$/SBA-15 were very small, only observing in a few nanometres. It is obvious that these nanoparticles reached superparamagnetic sizes. The magnetizations of samples were in the order of $CuFe_2O_4$_SG > $CuFe_2O_4$_TP > $CuFe_2O_4$/SBA-15. This could possibly result from the effect of particle size. As particle size decreases, the surface-to-volume ratio increases. The noncollinearity of the spins from the surface of the nanoparticles is reflected in the decrease of the saturation magnetization, as compared to that of the bulk material. The decrease of the saturation magnetization can be higher in ferrimagnetic nanoparticles, where the exchange interaction takes place through the oxygen ions (super exchange interaction).[27] Moreover, the variation in the saturation magnetization could also be influenced by the difference in the cation distribution among the tetrahedral and octahedral sites of the spinel $CuFe_2O_4$. It has been reported that the cation distribution in the spinel structure could be influenced by the particle size, the preparation method, the calcination temperature, and the cation-doping.[28–32] As the magnetic moments of cations located in the tetrahedral and octahedral sites couple in an antiparallel alignment, the net magnetization of the spinel ferrites is related to the difference between those of the octahedral and tetrahedral cations.[32] Accordingly, the change in the cation distribution can significantly affect the magnetic properties of materials, *e.g.*, saturation magnetization, coercivity and Curie temperature.[29,31] It is therefore important to gain the full structural information. The local structure and cation distribution of these $CuFe_2O_4$ spinel nanoparticles were further determined by XAS analysis. It is worth noting that with increasing particle size, the spin order of the existing elements on the surface was predominant and this corresponded to the affirmation of their magnetic property which could relate the catalytic activity.[2]

3.1.5 Local structure and cation distribution of $CuFe_2O_4$ spinel. The Fe K-edge XANES spectra of the reference compounds and the calcined $CuFe_2O_4$ catalysts are presented in Fig. 5. The XANES feature at Fe K-edge of standard $CuFe_2O_4$ sample was similar to that of Fe_3O_4 with the higher edge threshold energy. This indicated that the $CuFe_2O_4$ sample contained higher amount of Fe^{3+} species. However, as observed from all samples, there was no significant difference in spectral features compared to $CuFe_2O_4$ standard materials. Small absorption peaks at the pre-edge region were observed due to the electric quadrupole-allowing transitions of Fe species confirming the existence of Fe ions in the tetrahedral and octahedral sites. Normally, cuprospinel is an inverse spinel where Cu^{2+} only occupies in octahedral sites and iron ions (Fe^{2+} and Fe^{3+}) are equally distributed between the octahedral and tetrahedral sites in the structure.[33] The Fe^{2+} ions prefer to occupy octahedral sites while the Fe^{3+} ions prefer to occupy tetrahedral sites.[34] In EXAFS spectra (Fig. 6), the intensity of the first peak arises from the scattering of the nearest neighbour oxygen anions (Fe–O) while the second large peak is caused by the scattering of the Fe and Cu, possibly located in both tetrahedral and octahedral sites. The interatomic distance of the Fe–O and Fe–Fe bonds was insignificantly different in each sample. However, a variation of relative peak heights of these two major peaks was observed, which would indicate a significant change in the local structural environment of Fe ions in the $CuFe_2O_4$ catalysts prepared with three different synthesis methods. From the EXAFS analysis, the quantitative information on the cation distribution was illustrated in Table 1. In $CuFe_2O_4$_SG, Fe ions were almost equally distributed between the octahedral and tetrahedral sites, and all Cu ions should be located at the octahedral sites. For $CuFe_2O_4$_TP and $CuFe_2O_4$/SBA-15 samples, 63.4% and 84.3% of Fe ions respectively occupied octahedral sites, which would suggest that Cu ions were partly located at the octahedral and tetrahedral sites. It is clear that the cation distribution in $CuFe_2O_4$ spinel nanoparticles was strongly affected by preparation methods.

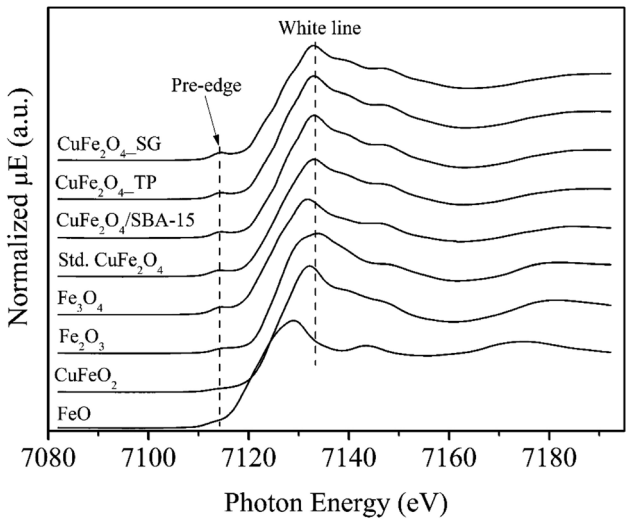

Fig. 5 Fe K-edge XANES spectra of $CuFe_2O_4$_SG, $CuFe_2O_4$_TP and $CuFe_2O_4$/SBA-15 samples compared with standard materials of $CuFe_2O_4$, Fe_3O_4, Fe_2O_3, $CuFeO_2$, and FeO.

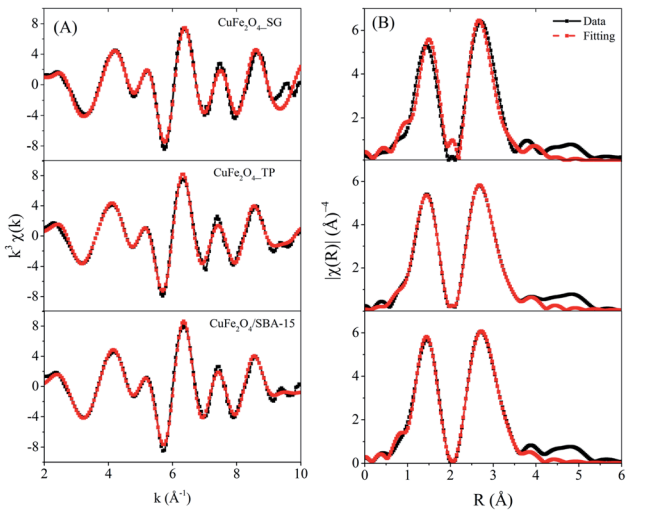

Fig. 6 (A) EXAFS oscillations, $k^3\chi(k)$, and (B) their Fourier transforms of $CuFe_2O_4$/SBA-15, $CuFe_2O_4$_TP and $CuFe_2O_4$_SG.

3.1.6 Reduction behaviours of $CuFe_2O_4$ spinel. In order to understand the transformation of $CuFe_2O_4$ spinel under the reduction condition, the H_2-TPR was particularly employed for the study. Illustrated in Fig. 7, two pronounced reduction regions were observed for each sample. It has been reported that the reduction peak at lower temperature range of 180–420 °C was responsible for the reduction of $CuFe_2O_4$ to Cu^0 and Fe_3O_4 species.[1] Subsequently, Fe_3O_4 is reduced to Fe^0 particles at higher temperature (420–750 °C). These results were in close agreement with those reported in literatures.[5,35] According to these results, it was difficult to identify a specific species during these two reduction steps. Normally, $CuFe_2O_4$ was mainly reduced to Cu and Fe_2O_3 by removing of the lattice oxygen under H_2 atmosphere, then Fe_2O_3 was rapidly reduced to Fe_3O_4.[33] For comparison with individual TPR profiles, it was found that $CuFe_2O_4$_TP and $CuFe_2O_4$_SG showed almost the same reduction temperature compared to $CuFe_2O_4$/SBA-15. The unsupported $CuFe_2O_4$ required higher temperature for its reduction process. In contrast, $CuFe_2O_4$/SBA-15 composite has a lowest reduction temperature for reducing $CuFe_2O_4$ to metallic copper and Fe_3O_4 oxide, indicating that metal supported materials was easier reduced than the bulk (unsupported) metal oxides. This phenomenon can be explained in term of specific surface area and H_2 spillover.[36] When the SBA-15 surface was completely covered by the dissociative adsorbed hydrogen atom, it spilled over the surface of SBA-15 and migrated to react with $CuFe_2O_4$. Hence, it increased the reduction to a higher rate. The lower reduction temperature of $CuFe_2O_4$/SBA-15 might be a result of the generation of nanometallic Cu active sites, which enhanced the catalytic properties.

To further investigate the reductive species in the reduced samples, Cu and Fe K-edges XANES spectra were collected and have been displayed in Fig. 8. In the Cu K-edge, the edge energies of the reduced samples are the same as the Cu foil, indicating the presence of metallic copper. A closer look at XANES spectra, the white line feature and shoulder were observed in $CuFe_2O_4$_SG, indicating dominating copper oxides in the samples. Here, the intense white line peak and the dominant shoulder in the $CuFe_2O_4$_SG could be assigned to the 1s → 4p transition of Cu_2O. To analyze the composition of copper species in the samples, the linear combination fit analysis was applied. The quantification by linear combination fitting yields a mixture of metallic Cu, Cu_2O and CuO in each sample (Fig. 8). It was found that the copper ions in $CuFe_2O_4$/SBA-15 were highly reduced to the state of zero, while the $CuFe_2O_4$_SG was partially reduced at 350 °C. In case of Fe K-edge, the XANES fit of Fe K-edge revealed that the catalysts were fully remained in the oxide forms. The structure of iron was gradually change from $CuFe_2O_4$ to typically iron oxides like FeO, Fe_3O_4, and Fe_2O_3. These results are consistent with the H_2-TPR which ascribe that iron species in $CuFe_2O_4$ spinel are more resistant toward reduction.

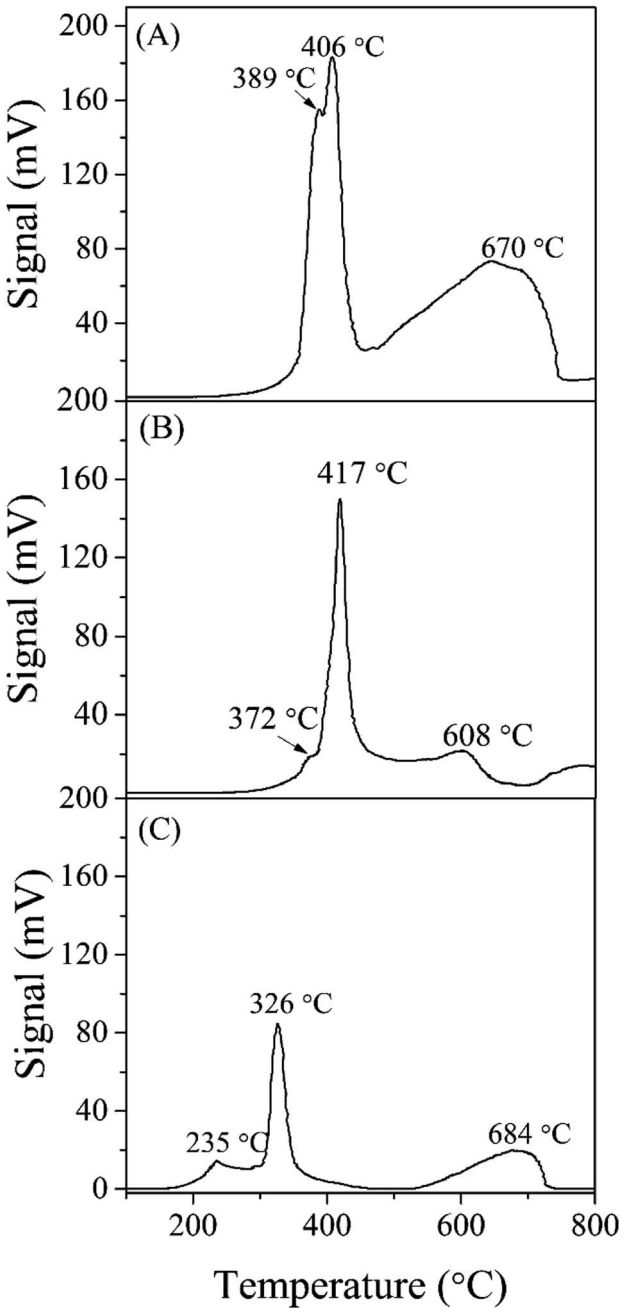

Fig. 7 TPR profiles of (A) $CuFe_2O_4$_SG, (B) $CuFe_2O_4$_TP, and (C) $CuFe_2O_4$/SBA-15.

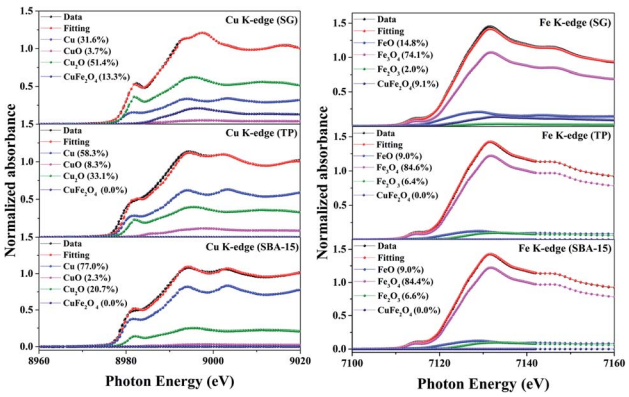

Fig. 8 Linear combination fitted-XANES spectra of $CuFe_2O_4$/SBA-15, $CuFe_2O_4$_TP, and $CuFe_2O_4$_SG after reduction under H_2 atmosphere.

3.2 Testing of $CuFe_2O_4$ spinel for steam reforming of methanol (SRM)

Prior to demonstrate the catalytic performance, the blank test of pure siliceous SBA-15 was carried out with the same space velocity. The result showed a negligible catalytic activity of the siliceous SBA-15. In Fig. 9, the catalytic results of each catalyst were represented in the term of H_2 production rate and methanol conversion as a function of temperature. After H_2 reduction at 350 °C, it was observed that the rate of methanol conversion and H_2 production rate per gram of catalyst were in order of $CuFe_2O_4$_SG > $CuFe_2O_4$/SBA-15 > $CuFe_2O_4$_TP. However, when considering the H_2 production rate per gram of active $CuFe_2O_4$ spinel, the $CuFe_2O_4$/SBA-15 catalyst showed the highest H_2 production rate (~5500 mol $kg_{(CuFe2O4)}^{-1}$ h^{-1}) at the reaction temperature of 375 °C. It is suggested that the improved turnover rate of $CuFe_2O_4$/SBA-15 was due to the high dispersion of copper spinel particles on the SBA-15 support. Moreover, the mesoporous SBA-15 silica support could obstruct the sintering process of nano-metallic copper during the reaction and enhanced the catalytic reaction.

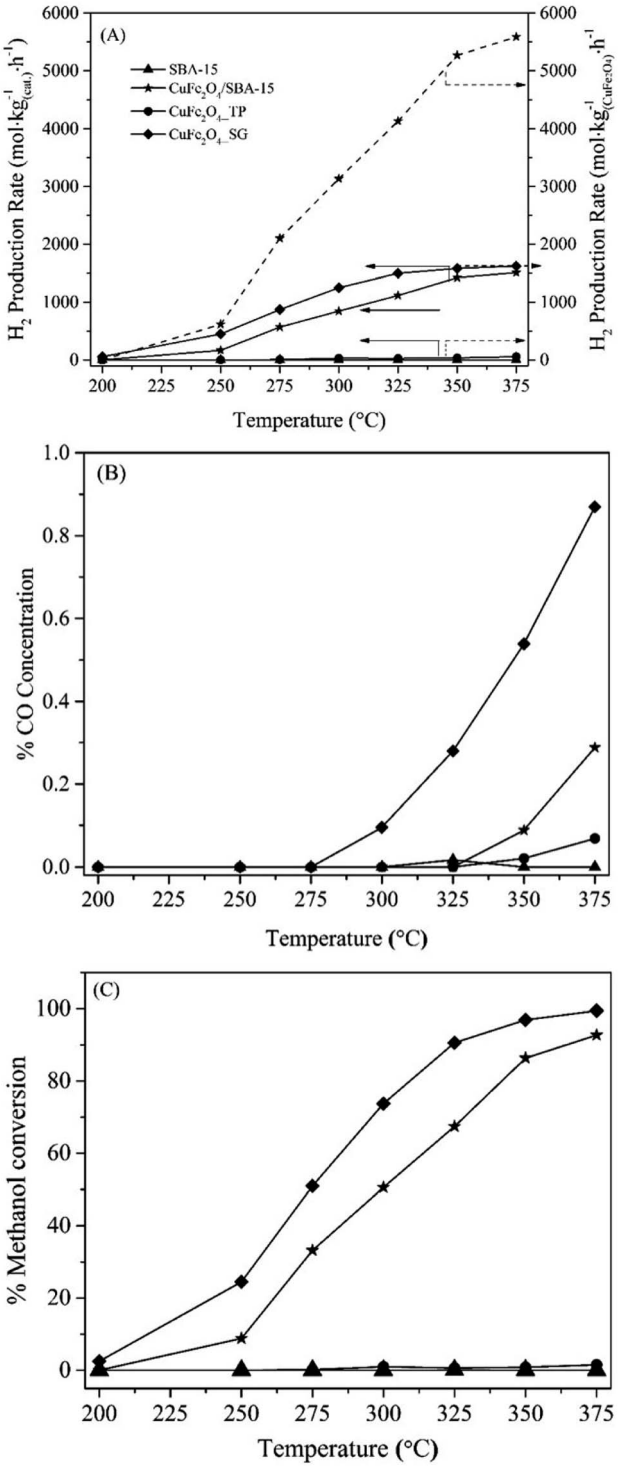

Fig. 9 (A) H_2 production rate, (B) % methanol conversion, and (C) % CO concentration of samples.

Comparison between $CuFe_2O_4$_SG and $CuFe_2O_4$_TP catalysts, it was very interesting that the lower surface of $CuFe_2O_4$_SG provided the highest catalytic activity (100% conversion and H_2 production rate of ~1600 mol kg_{Cat}^{-1} h^{-1} at 375 °C) compared to the higher surface area of $CuFe_2O_4$_TP. The $CuFe_2O_4$_TP exhibits the lowest yield of H_2 production rate (<10 mol kg_{Cat}^{-1} h^{-1}) with % methanol conversion of less than 1%. This result suggested that almost no metallic copper was generated from the reduction of the needle-like $CuFe_2O_4$_TP. To verify this concept, the catalytic evaluation of $CuFe_2O_4$_SG and $CuFe_2O_4$_TP was also studied under the reduction temperature of 420 °C as indicated by TPR results that $CuFe_2O_4$_SG and $CuFe_2O_4$_TP catalysts could be completely reduced at temperature higher than 350 °C. However, the catalytic activity of these two catalysts after reducing at 420 °C was dramatically decreased in their performance. This could be attributed to the fact that the reduced copper was sintered to form bulky particles during the reduction process. Hence, the reduction temperature at 350 °C was enough for reduction of $CuFe_2O_4$_SG and $CuFe_2O_4$_TP in this reaction. Nevertheless, it was an unexpected result that the needle-like $CuFe_2O_4$_TP was not active for the methanol steam reforming. This issue should be further investigated and reported in next.

4. Conclusions

The preparation methods strongly affected on cation distribution and physicochemical properties of $CuFe_2O_4$. The $CuFe_2O_4$ supported on SBA-15 exhibited the superparamagnetic behaviour with well-crystallized tetragonal structure and high reducibility. However, upon removal of SBA-15 from the $CuFe_2O_4$/SBA-15, the needle-like of $CuFe_2O_4$_TP with high surface area, but the reduction requires a high temperature as well as sol–gel combustion method.

Conflicts of interest

There are no conflicts to declare.

Acknowledgements

This work was supported by the Thailand Research Fund (TRF) and NANOTEC through the Young Research Grants to Pongtanawat Khemthong (Grant No. TRG5780192). This work was also

conducted under the research on development of novel technologies for safe agriculture by Faculty of Engineering, Khon Kaen University which has received funding support from Fundamental Fund 2022 (the National Science, Research and Innovation Fund (NSRF), Thailand).

Notes and references

1 S. Kameoka, T. Tanabe and A. P. Tsai, *Catal. Lett.*, 2005, **100**, 89–93.
2 K. Faungnawakij, N. Shimoda, T. Fukunaga, R. Kikuchi and K. Eguchi, *Appl. Catal., B*, 2009, **92**, 341–350.
3 K. Faungnawakij, N. Shimoda, N. Viriya-empikul, R. Kikuchi and K. Eguchi, *Appl. Catal., B*, 2010, **97**, 21–27.
4 N. Shimoda, K. Faungnawakij, R. Kikuchi and K. Eguchi, *Appl. Catal., A*, 2010, **378**, 234–242.
5 K. Faungnawakij, N. Shimoda, T. Fukunaga, R. Kikuchi and K. Eguchi, *Appl. Catal., A*, 2008, **341**, 139–145.
6 J. Papavasiliou, G. Avgouropoulos and T. Ioannides, *Catal. Commun.*, 2005, **6**, 497–501.
7 S. Patel and K. Pant, *J. Porous Mater.*, 2006, **13**, 373–378.
8 S.-C. Yang, W.-N. Su, S. D. Lin, J. Rick, J.-H. Cheng, J.-Y. Liu, C.-J. Pan, D.-G. Liu, J.-F. Lee and T.-S. Chan, *Appl. Catal., B*, 2011, **106**, 650–656.
9 K. Faungnawakij and N. Viriya-Empikul, *Appl. Catal., A*, 2010, **382**, 21–27.
10 W. Yue and W. Zhou, *Chem. Mater.*, 2007, **19**, 2359–2363.
11 H. Yen, Y. Seo, R. Guillet-Nicolas, S. Kaliaguine and F. Kleitz, *Chem. Commun.*, 2011, **47**, 10473–10475.
12 M.-b. Zheng, J. Cao, S.-t. Liao, J.-s. Liu, H.-q. Chen, Y. Zhao, W.-j. Dai, G.-b. Ji, J.-m. Cao and J. Tao, *J. Phys. Chem. C*, 2009, **113**, 3887–3894.
13 A.-H. Lu and F. Schüth, *C. R. Chim.*, 2005, **8**, 609–620.
14 C. D. Sewell, Z. Wang, Y.-W. Harn, S. Liang, L. Gao, X. Cui and Z. Lin, *J. Mater. Chem. A*, 2021, **9**, 20375–20384.
15 L. Gao, X. Cui, Z. Wang, C. D. Sewell, Z. Li, S. Liang, M. Zhang, J. Li, Y. Hu and Z. Lin, *Proc. Natl. Acad. Sci. U. S. A.*, 2021, **118**, e2023421118.
16 X. Li, J. Iocozzia, Y. Chen, S. Zhao, X. Cui, W. Wang, H. Yu, S. Lin and Z. Lin, *Angew. Chem., Int. Ed.*, 2018, **57**, 2046–2070.
17 V. Meynen, P. Cool and E. Vansant, *Microporous Mesoporous Mater.*, 2009, **125**, 170–223.
18 P. Kidkhunthod, *Adv. Nat. Sci.: Nanosci. Nanotechnol.*, 2017, **8**, 035007.
19 M. Newville, *J. Synchrotron Radiat.*, 2001, **8**, 96–100.
20 B. Ravel and M. Newville, *J. Synchrotron Radiat.*, 2005, **12**, 537–541.
21 M. G. Sorolla, M. L. Dalida, P. Khemthong and N. Grisdanurak, *J. Environ. Sci.*, 2012, **24**, 1125–1132.
22 C. Luadthong, P. Khemthong, W. Nualpaeng and K. Faungnawakij, *Appl. Catal., A*, 2016, **525**, 68–75.
23 G. Tompsett, L. Krogh, D. Griffin and W. Conner, *Langmuir*, 2005, **21**, 8214–8225.
24 B. Issa, I. M. Obaidat, B. A. Albiss and Y. Haik, *Int. J. Mol. Sci.*, 2013, **14**, 21266–21305.
25 P. Laokul, V. Amornkitbamrung, S. Seraphin and S. Maensiri, *Curr. Appl. Phys.*, 2011, **11**, 101–108.
26 R. Yadav, I. Kuřitka, J. Vilčáková, J. Havlica, J. Másilko, L. Kalina, J. Tkacz, M. Hajdúchová and V. Enev, *Structural, dielectric, electrical and magnetic properties of $CuFe_2O_4$ nanoparticles synthesized by honey mediated sol–gel combustion method and annealing effect*, 2017.
27 C. Caizer and M. Rai, *Magnetic Nanoparticles in Human Health and Medicine: Current Medical Applications and Alternative Therapy of Cancer*, Wiley, 2021.
28 V. Blanco-Gutiérrez, F. Jiménez-Villacorta, P. Bonville, M. J. Torralvo-Fernández and R. Sáez-Puche, *J. Phys. Chem. C*, 2011, **115**, 1627–1634.
29 S. Calvin, M. Shultz, L. Glowzenski and E. Carpenter, *J. Appl. Phys.*, 2010, **107**, 024301.
30 T. Tangcharoen, W. Klysubun, J. T-Thienprasert and C. Kongmark, *J. Solid State Chem.*, 2020, **292**, 121695.
31 S. Patange, S. E. Shirsath, G. Jangam, K. Lohar, S. S. Jadhav and K. Jadhav, *J. Appl. Phys.*, 2011, **109**, 053909.
32 P. Khemthong, C. Kongmark, N. Kochaputi, S. Mahakot, S. Rodporn and K. Faungnawakij, *Inorg. Chem.*, 2019, **58**, 6584–6587.
33 M. Estrella, L. Barrio, G. Zhou, X. Wang, Q. Wang, W. Wen, J. C. Hanson, A. I. Frenkel and J. A. Rodriguez, *J. Phys. Chem. C*, 2009, **113**, 14411–14417.
34 V. Krishnan, R. K. Selvan, C. O. Augustin, A. Gedanken and H. Bertagnolli, *J. Phys. Chem. C*, 2007, **111**, 16724–16733.
35 S. Kameoka, T. Tanabe and A. P. Tsai, *Appl. Catal., A*, 2010, **375**, 163–171.
36 N. Iwasa and N. Takezawa, *Top. Catal.*, 2003, **22**, 215–224.